



**HAL**  
open science

## From electron tomography of dislocations to field dislocation mechanics: application to olivine

Timmo Weidner, Vincent Taupin, Sylvie Demouchy, Karine Gouriet, Antoine Guitton, Patrick Cordier, Alexandre Mussi

### ► To cite this version:

Timmo Weidner, Vincent Taupin, Sylvie Demouchy, Karine Gouriet, Antoine Guitton, et al.. From electron tomography of dislocations to field dislocation mechanics: application to olivine. Modelling and Simulation in Materials Science and Engineering, 2023, 32 (1), pp.015004. 10.1088/1361-651X/ad0a42 . hal-04276564

**HAL Id: hal-04276564**

**<https://uca.hal.science/hal-04276564>**

Submitted on 9 Nov 2023

**HAL** is a multi-disciplinary open access archive for the deposit and dissemination of scientific research documents, whether they are published or not. The documents may come from teaching and research institutions in France or abroad, or from public or private research centers.

L'archive ouverte pluridisciplinaire **HAL**, est destinée au dépôt et à la diffusion de documents scientifiques de niveau recherche, publiés ou non, émanant des établissements d'enseignement et de recherche français ou étrangers, des laboratoires publics ou privés.



Distributed under a Creative Commons Attribution 4.0 International License

ACCEPTED MANUSCRIPT • OPEN ACCESS

## From Electron Tomography of Dislocations to Field Dislocation Mechanics: Application to Olivine

To cite this article before publication: Timmo Weidner *et al* 2023 *Modelling Simul. Mater. Sci. Eng.* in press <https://doi.org/10.1088/1361-651X/ad0a42>

### Manuscript version: Accepted Manuscript

Accepted Manuscript is “the version of the article accepted for publication including all changes made as a result of the peer review process, and which may also include the addition to the article by IOP Publishing of a header, an article ID, a cover sheet and/or an ‘Accepted Manuscript’ watermark, but excluding any other editing, typesetting or other changes made by IOP Publishing and/or its licensors”

This Accepted Manuscript is © 2023 The Author(s). Published by IOP Publishing Ltd.



As the Version of Record of this article is going to be / has been published on a gold open access basis under a CC BY 4.0 licence, this Accepted Manuscript is available for reuse under a CC BY 4.0 licence immediately.

Everyone is permitted to use all or part of the original content in this article, provided that they adhere to all the terms of the licence <https://creativecommons.org/licenses/by/4.0>

Although reasonable endeavours have been taken to obtain all necessary permissions from third parties to include their copyrighted content within this article, their full citation and copyright line may not be present in this Accepted Manuscript version. Before using any content from this article, please refer to the Version of Record on IOPscience once published for full citation and copyright details, as permissions may be required. All third party content is fully copyright protected and is not published on a gold open access basis under a CC BY licence, unless that is specifically stated in the figure caption in the Version of Record.

View the [article online](#) for updates and enhancements.

1  
2  
3 **From Electron Tomography of Dislocations to Field Dislocation Mechanics:**  
4  
5 **Application to Olivine**  
6  
7  
8  
9

10 Timmo WEIDNER<sup>1</sup>, Vincent TAUPIN<sup>2,3</sup>, Sylvie DEMOUCHEY<sup>4,5</sup>, Karine GOURIET<sup>1</sup>,  
11 Antoine GUITTON<sup>2,3</sup>, Patrick CORDIER<sup>1,6</sup>, Alexandre MUSSI<sup>1\*</sup>  
12  
13

14 <sup>1</sup>*Univ. Lille, CNRS, INRAE, Centrale Lille, UMR 8207 - UMET - Unité Matériaux et*  
15  
16 *Transformations, F-59000 Lille, France*  
17  
18

19 <sup>2</sup>*Université de Lorraine, CNRS, Arts et Métiers, LEM3, Metz, 57070, France*  
20

21 <sup>3</sup>*LabEx DAMAS, Université de Lorraine, Metz, 57070, France*  
22

23 <sup>4</sup>*Geosciences Montpellier, Université de Montpellier & CNRS, UMR 5243, F-34095*  
24 *Montpellier, France*  
25  
26

27 <sup>5</sup>*Laboratoire Magmas et Volcans, Université Clermont Auvergne, CNRS, IRD & OPGC,*  
28 *UMR 6524, F-63170 Aubière, France*  
29  
30

31 <sup>6</sup>*Institut Universitaire de France, F-75005 Paris, France*  
32  
33

34  
35  
36  
37  
38  
39  
40  
41 Corresponding author: [alexandre.mussi@univ-lille.fr](mailto:alexandre.mussi@univ-lille.fr)  
42  
43  
44  
45  
46  
47  
48  
49  
50  
51  
52  
53  
54  
55  
56  
57  
58  
59  
60

## 1 **Abstract**

2 We propose a new procedure to extract information from electron tomography and use them as  
3 an input in a field dislocation mechanics. Dislocation electron tomography is an experimental  
4 technique that provides three-dimensional information on dislocation lines and Burgers vectors  
5 within a thin foil. The characterized 3D dislocation lines are used to construct the spatial  
6 distribution of the equivalent Nye dislocation density tensor. The model dislocation lattice  
7 incompatibility equation and stress balance equation are solved with a spectral code based on  
8 fast Fourier transform algorithms. As an output of the model, one obtains the three-dimensional  
9 distribution of mechanical fields, such as strains, rotations, stresses, resolved shear stresses and  
10 energy, inside the material. To assess the potential of the method, we consider two regions from  
11 a previously compressed olivine sample. Our results reveal significant local variations in local  
12 stress fields and resolved shear stresses in various slip systems, which can impact the strong  
13 plastic anisotropy of olivine and the activation of different dislocation slip systems. It also  
14 evidences the built-up of kinematic hardening down to the nanometre scale.

15  
16 **Keywords:** Dislocations; Electron Tomography; Mechanics; Plasticity; Olivine

## 17 18 **1 Introduction**

19 Making the link between plastic flow and the dynamics of crystal defects (dislocations) that  
20 causes it is a formidable challenge that requires the description of their collective behaviour at  
21 the mesoscopic scale [1]. To this end, mesoscopic simulations such as discrete dislocation  
22 dynamics (DDD) [2, 3] represent a powerful analysis tool that should be complementary to  
23 experimental observations of dislocations. Complementary experimental/modelling analysis of  
24 dislocation microstructures can bring valuable insights about elementary deformation  
25 mechanisms. Transmission electron microscopy is usually the experimental tool of choice for

1  
2  
3 26 this kind of investigation since it allows a fine characterization of dislocations and their  
4  
5 27 interactions. However, the understanding of the 3D microstructures is difficult since we only  
6  
7 28 have access to 2D projections and the tilt capabilities are physically limited in microscopes.  
8  
9 29 Dislocation Electron Tomography (DET) has been developed to overcome these limitations.  
10  
11 30 The basic principle as originally proposed by Barnard *et al.* (2006) [4] is to perfectly orient the  
12  
13 31 diffraction vector used to image the dislocations parallel to the tilt axis, maintaining at best as  
14  
15 32 possible the Bragg deviation parameter. This technique has been applied in numerous studies  
16  
17 33 as analyses of dislocation microstructures near cracks [5, 6], characterization of helical  
18  
19 34 configurations of dislocations [7-9], analyses of specific interactions of dislocations [10],  
20  
21 35 studies of interactions of dislocations with grain and sub-grain boundaries [11-14], analyses of  
22  
23 36 dislocation microstructures in a carbide [15] and minerals [16-19]. The DET has been the  
24  
25 37 subject of several recent reviews [20-23]. Recent developments include reconstructions from  
26  
27 38 few projected images using black & white contrasts of dislocations [9, 19] or “stereo-pair”  
28  
29 39 method [24-27], machine-learning reconstruction [28] and 4D analysis [9]. In the present  
30  
31 40 contribution, we propose to use electron tomography to get access to the line directions of the  
32  
33 41 dislocation segments. The association of these line directions with their corresponding Burgers  
34  
35 42 vectors allows the construction of the Nye dislocation density tensor at any point in the  
36  
37 43 reconstructed space. Subsequently, the Nye dislocation density tensor leads up to the prediction  
38  
39 44 of the internal mechanical fields (strain, stress, energy, etc.) through the use of a Field  
40  
41 45 Dislocation Mechanics (FDM) model that allows to build a bridge between real dislocation  
42  
43 46 microstructures and continuum mechanics. To illustrate the potential of this DET/FDM analysis  
44  
45 47 method, we consider here as a benchmark the characterization of dislocation networks in an  
46  
47 48 experimentally deformed olivine sample. We will consider in this work two different areas from  
48  
49 49 a deformed single crystal. We reveal for this complex material (limited number of dislocation  
50  
51 50 slip systems, strong plastic anisotropy) a three-dimensional stress state characterized by  
52  
53  
54  
55  
56  
57  
58  
59  
60

1  
2  
3 51 significant spatial variations and long-range elastic interactions between dislocations. The  
4  
5 52 resulting distribution of dislocation driving stresses allows suggesting possible active slip  
6  
7 53 systems and the strong heterogeneity of distributions shows that the history of dislocation  
8  
9 54 dynamics and the associated build-up of kinematic hardening can be captured with the proposed  
10  
11 55 method.  
12  
13  
14  
15  
16  
17

## 18 57 **2 Materials and deformation experiments**

19  
20 58 This study was carried out on an olivine sample (PoEM9) experimentally deformed by  
21  
22 59 Demouchy *et al.* (2013) [29] which had already been the focus of TEM microstructural  
23  
24 60 investigations [10, 17]. These axial compression experiments were carried out on a cylinder  
25  
26 61 (length 6.32 mm; diameter 4.19 mm) specimen extracted from a large, gem-quality, single  
27  
28 62 crystal of San Carlos olivine ( $(\text{Mg}_{0.91}\text{Fe}_{0.09}\text{Ni}_{0.003})_2\text{SiO}_4$ ). The sample PoEM9 [29], was  
29  
30 63 deformed along [502] in a high-resolution gas-medium high-pressure apparatus [30] at 806 °C,  
31  
32 64 with a constant strain rate of  $5.1 \times 10^{-5} \text{ s}^{-1}$ , under a gaseous (Ar) confining pressure of 300 MPa.  
33  
34  
35 65 The finite strain reached was  $\epsilon_{Total} = 10.1 \%$  (obtained post-mortem) and the maximum  
36  
37 66 differential stress was 754 MPa.  
38  
39  
40  
41  
42

## 43 68 **3 Methods**

### 44 69 ***3.1 Transmission electron microscopy***

45  
46  
47 70 A complete characterization of the dislocations must include not only the Burgers vectors, but  
48  
49 71 also the geometry of the lines and their habit planes.

#### 50 72 ***3.1.a Indexation of Burgers vectors***

51  
52  
53 73 In the earlies 1980s, Ishida *et al.* [31] have shown that the product of the Burgers vectors  $\mathbf{b}$  of  
54  
55 74 a dislocation and of the diffraction vector  $\mathbf{g}$  used to perform the weak-beam dark-field (WBDF)  
56  
57 75 image is equal to the number of thickness fringes which ends at the extremity of this considered  
58  
59  
60

1  
2  
3 76 dislocation (the direction of the ending thickness fringes is linked to the sign of the Burgers  
4  
5 77 vector [32]).

6  
7  
8 78 Figure 1 gives an example of a typical WBDF micrograph of PoEM9 where the diffraction  
9  
10 79 vector  $\mathbf{g}$ : 004 was used to image dislocations (this reflection was chosen as it has the highest  
11  
12 80 structure factor in olivine). The  $\mathbf{g} \cdot \mathbf{b}$  product is equal to  $\pm 4$  with a  $\pm[001]$  Burgers vector. This  
13  
14 81 number clearly corresponds to the number of terminating thickness fringes seen on figure 1b  
15  
16  
17 82 and 1c.

18  
19 83 Figure 1

20  
21 84 Asymmetry of the contrast intensity of dislocation extremities is linked to the sign of the  
22  
23  
24 85 Burgers vectors. This information can be compared to the one obtained from the directions of  
25  
26 86 terminating thickness fringes (Figure 2). Taking all these indices into account, we were able to  
27  
28 87 determine most of the Burgers vector signs.

29  
30  
31 88 Figure 2

### 32 33 89 **3.1.b Dislocation geometry characterization**

34  
35 90 The electron tomography technique entails acquiring a tilt-series and then utilizing a  
36  
37 91 reconstruction algorithm to obtain a corresponding three-dimensional (3D) model of the  
38  
39 92 microstructure. As outlined in prior studies [8, 16], the principal impediment to performing  
40  
41 93 electron tomography of dislocations is to maintain a diffraction contrast (which is highly  
42  
43 94 sensitive to the thin foil orientation) constant across the tilt-series. In order to address this issue,  
44  
45 95 the diffraction vector, used to image dislocations, must be precisely aligned with the principal  
46  
47 96 axis of the sample-holder. Furthermore, a slight precession of the electron beam is applied to  
48  
49 97 homogenize the background contrasts (including the presence of thickness fringes) and the  
50  
51 98 dislocation contrasts (oscillating contrasts of dislocations which cross the thin foil thickness)  
52  
53 99 [16, 33]. To enhance the dislocation contrasts, a numerical filter has been employed in ImageJ  
54  
55  
56  
57  
58 100 to adjust the contrast. Reconstructions are then conducted with the weighted back-projection  
59  
60

1  
2  
3 101 algorithm [34], while dislocations are directly redrawn into the reconstructed volume using  
4  
5 102 markers, facilitated by the Chimera-UCSF software [8, 9, 15, 18-20, 35], to attain precisely the  
6  
7 103 3D coordinates of the dislocation core images.

### 104 *3.2 Nye tensor and elastic field distribution in an anisotropic elastic material*

105 The Field Dislocation Mechanics (FDM) model employed here [36] introduces discrete  
106 dislocation lines, as characterized by tomography, in the form of equivalent continuous  
107 dislocation density spatial distributions on a regular three-dimensional grid made of voxels. As  
108 an output, the model provides the equilibrated stress field in the voxelized thin foil volume, as  
109 well as the associated elastic displacements, strains, and rotations. The characteristics of  
110 dislocations, namely their line directions and their Burgers vectors, are introduced through the  
111 Nye dislocation tensor in the model [37]. The Nye tensor  $\alpha$  is a second-order tensor with  
112 components  $\alpha_{ij} = B_i t_j$  in the cartesian coordinate system ( $\mathbf{e}_1, \mathbf{e}_2, \mathbf{e}_3$ ) aligned with the thin foil  
113 frame. The quantity  $B_i$  is a length of Burgers vector per unit surface and can be written  $B_i =$   
114  $nb/\Delta_S \mathbf{e}_i$ , where  $n$  is the number (not necessarily an integer) of dislocations of Burgers vector  
115 magnitude  $b$  along the direction  $\mathbf{e}_i$ , and  $\Delta_S$  is the spatial resolution surface. The vector  $\mathbf{t}$  is the  
116 local dislocation line unit vector. For instance, an edge (respectively screw) dislocation with  
117 line along the  $\mathbf{e}_3$  direction and with Burgers vector along the  $\mathbf{e}_1$  (respectively  $\mathbf{e}_3$ ) direction  
118 corresponds to an edge (respectively screw) dislocation density  $\alpha_{13}$  (respectively  $\alpha_{33}$ ). A mixed  
119 dislocation would be made of both densities. In practice, any three-dimensional dislocation line  
120 or segment can be transferred into an equivalent Nye dislocation density distribution in a  
121 volume. In the case of a regular grid made of voxels to be used later for fast Fourier transform  
122 (FFT) based numerical calculation of elastic fields, we use the recent method proposed by  
123 Bertin [38] to transform discrete dislocation segments into equivalent dislocation densities  
124 properly assigned on voxels. Note that a similar approach was also proposed very recently [39].



1  
2  
3 125 The method used is briefly presented below, the reader is referred to reference [38] for more  
4  
5 126 details.

7  
8 127 Figure 3

9  
10 128 Figure 3 illustrates a part of a discrete dislocation line composed of three straight segments  
11  
12 129 shown in red in the figure. The figure shows a two-dimensional setup for clarity, but the  
13  
14 130 calculation is performed in three dimensions. The second (middle) dislocation segment is  
15  
16 131 considered here and shown as a bold red line. It is defined by its starting point,  $\mathbf{x}_a$ , and its ending  
17  
18 132 point,  $\mathbf{x}_b$ , following the direction of the segment line vector  $\mathbf{t}$ . The thin dashed black lines  
19  
20 133 delimit the grid voxels used in the numerical algorithm used to solve FDM equations. The voxel  
21  
22 134 size is  $H_1$ ,  $H_2$ , and  $H_3$  in the  $\mathbf{x}_1$ ,  $\mathbf{x}_2$ , and  $\mathbf{x}_3$  directions. The position of the centre of voxel  $d$   
23  
24 135 considered in the figure is given by its position vector  $\mathbf{x}_d$ . Its volume is denoted  $\Omega_d =$   
25  
26 136  $H_1 \times H_2 \times H_3 = H^3$  where we chose that  $H_1 = H_2 = H_3 = H$ . For the voxel  $d$ , a surrounding  
27  
28 137 box of dimension  $2H_1 \times 2H_2 \times 2H_3$  is centered at point  $\mathbf{x}_d$  and is shown with purple solid lines  
29  
30 138 in the figure. If a part of a given dislocation segment falls within this box, then a Nye dislocation  
31  
32 139 density associated with this segment will be attributed to this voxel, as follows. If start and/or  
33  
34 140 end points  $\mathbf{x}_a/\mathbf{x}_b$  are outside the box, the dislocation segment is cropped to new start and/or end  
35  
36 141 points  $\mathbf{x}_a'/\mathbf{x}_b'$ . If they are inside, they remain as they are. Now consider a point  $\mathbf{x}$  along the  
37  
38 142 dislocation segment. We define the vector  $\mathbf{R}_d = \mathbf{x}_d - \mathbf{x}$ , which brings points  $\mathbf{x}$  on the segment to  
39  
40 143 the centre of voxel  $\mathbf{x}_d$ . The unit vector  $\mathbf{t} = (\mathbf{x}_b - \mathbf{x}_a) / \|\mathbf{x}_b - \mathbf{x}_a\|$  is the segment tangent vector. The  
41  
42 144 distance from the segment supporting line to point  $\mathbf{x}_d$  is denoted  $d$ . It is the norm of the vector  
43  
44 145  $\mathbf{d} = \mathbf{R}_d - (\mathbf{R}_d \cdot \mathbf{t})\mathbf{t} = \mathbf{x}_d - \mathbf{x}_0$ . The vector  $\mathbf{d}$  starts at point  $\mathbf{x}_0$  on the segment supporting line and ends at  
45  
46 146 point  $\mathbf{x}_d$ . With this, one can parametrize the position  $\mathbf{x}$  along the dislocation segment as  $\mathbf{x} = \mathbf{x}_0 + s\mathbf{t}$ ,  
47  
48 147 where the scalar value  $s \in [s_a, s_b]$ . The two bounds  $s_a$  and  $s_b$  shown in the figure ( $s_a'$  and/or  $s_b'$  if  
49  
50 148 the segment is cropped) are  $s_a = (\mathbf{x}_a - \mathbf{x}_0) \cdot \mathbf{t}$  and  $s_b = (\mathbf{x}_b - \mathbf{x}_0) \cdot \mathbf{t}$ . From these definitions, one can finally

1  
2  
3 149 parametrize the position vector  $\mathbf{R}_d = \mathbf{x}_d - \mathbf{x}$  as  $\mathbf{R}_d = \mathbf{d} \cdot \mathbf{st}$ . The dislocation density at the voxel  $d$  due  
4  
5 150 to a dislocation segment is given by the following line integral

$$151 \quad \alpha_{ij}(x_d) = \frac{b_i t_j}{\Omega_d} \int_{x_a}^{x_b} S(x_d - x) dL(x) = \frac{b_i t_j}{\Omega_d} I(x_d), \quad (1)$$

10  
11 152 where the weight function  $S$  is taken to be a Cloud-In-Cell function defined by

$$153 \quad S(x_d - x) = \begin{cases} \prod_{i=1}^3 \left(1 - \frac{|x_i^d - x_i|}{H_i}\right) & \text{if } |x_i^d - x_i| < H_i, \\ 0 & \text{otherwise.} \end{cases} \quad (2)$$

18 154 The integral  $I(x_d)$  can be numerically evaluated as

$$20 \quad I(x_d) = (s^b - s^a) - A_1 - A_2 - A_3 + B_{12} + B_{13} + B_{23} - C_{123}, \quad (3)$$

23 156 with the terms

$$25 \quad \left\{ \begin{array}{l} A_i = \frac{1}{H_i} \left| \left[ d_i s - \frac{1}{2} t_i s^2 \right]_a^b \right|, \\ B_{ij} = \frac{1}{H_i H_j} \left| \left[ d_i d_j s - \frac{1}{2} (d_i t_j + t_i d_j) s^2 + \frac{1}{3} t_i t_j s^3 \right]_a^b \right|, \\ C_{ijk} = \frac{1}{H_i H_j H_k} \left| \left[ d_i d_j d_k s - \frac{1}{2} (t_i d_j d_k + d_i t_j d_k + d_i d_j t_k) s^2 \right. \right. \\ \left. \left. + \frac{1}{3} (d_i t_j t_k + t_i d_j t_k + t_i t_j d_k) s^3 - \frac{1}{4} t_i t_j t_k s^4 \right]_a^b \right|. \end{array} \right. \quad (4)$$

36 158 The domain  $[s_a, s_b]$  is divided into portions  $[a, b]$  on which the sign of  $\prod_{i=1}^n (d_i - st_i)$  does not  
37  
38 159 change. For each voxel  $d$ , the dislocation density is the sum of all densities due to all dislocation  
39  
40 160 segments that cross the surrounding box shown in figure 3. The process is repeated for all voxels  
41  
42 161 forming the simulation volume. Given an initial Nye dislocation density in a volume, we are  
43  
44 162 now interested in numerically estimating the associated internal stress field within a small strain  
45  
46 163 anisotropic elasticity mechanical framework. We rely on the FDM model [36]. We denote by  
47  
48 164  $\mathbf{U}_e$  the elastic distortion of a three-dimensional body containing dislocations. In the absence of  
49  
50 165 dislocations, the distortion would be the gradient of the elastic displacement vector  $\mathbf{u}_e$ , that is  
51  
52 166  $\mathbf{U}_e = \mathbf{grad}(\mathbf{u}_e)$ . However, it is not true anymore in the presence of dislocations due to  
53  
54 167 discontinuities in the elastic displacement field, i.e., the Burgers vectors of dislocations. As

1  
2  
3 168 such, the elastic distortion must contain an incompatible, non-gradient, curl part ( $\mathbf{curl}(\boldsymbol{\chi})$ ),  
4  
5 169 which is related to the Nye tensor. The elastic distortion is thus written as

$$170 \quad \mathbf{U}_e = \mathbf{U}_e^{\parallel} + \mathbf{U}_e^{\perp} = \mathbf{grad}(\mathbf{u}_e) + \mathbf{curl}(\boldsymbol{\chi}). \quad (5)$$

171 The elastic distortion resumes to the compatible, gradient part, in the absence of dislocations,  
172 while the incompatible, curl part, is related to the Nye tensor through the incompatibility  
173 equation

$$174 \quad \mathbf{curl}(\mathbf{U}_e^{\perp}) = \boldsymbol{\alpha} = \mathbf{curl}(\mathbf{curl}(\boldsymbol{\chi})), \quad (6)$$

175 Where the curl operator removes the compatible part of the elastic distortion. For a given  
176 distribution of Nye dislocation density in a volume, the elastic incompatible distortion is  
177 obtained from the solution of equation (6). Then, the compatible elastic distortion is generally  
178 nonzero and ensures the balance of stresses inside the volume. That writes

$$179 \quad \mathbf{div}(\boldsymbol{\sigma}) = \mathbf{div}(\mathbf{C} : \mathbf{U}_e) = \mathbf{div}(\mathbf{C} : (\mathbf{U}_e^{\parallel} + \mathbf{U}_e^{\perp})) = \mathbf{0}, \quad (7)$$

180 where  $\boldsymbol{\sigma}$  is the Cauchy stress tensor and  $\mathbf{C}$  is the fourth-order elastic moduli tensor. The above  
181 equation can be rearranged as

$$182 \quad \mathbf{div}(\mathbf{C} : \mathbf{grad}(\mathbf{u}_e)) = -\mathbf{div}(\mathbf{C} : (\mathbf{U}_e^{\perp})), \quad (8)$$

183 and solved for the elastic displacement field  $\mathbf{u}_e$ . Once the elastic displacement is known, the  
184 compatible elastic distortion is obtained from its gradient and the total elastic distortion is  
185 finally obtained by adding the incompatible part. The total, balanced, stress field  $\boldsymbol{\sigma}$  is then  
186 obtained by multiplication by the elastic stiffness tensor  $\mathbf{C}$ . Solving equations (6-8) for a given  
187 distribution of Nye tensor provides a unique solution for the associated internal stress field [40].

188 Numerical solutions can be obtained from finite element approximations [41] and from spectral  
189 methods [42]. The latter rely on the use of fast Fourier transform (FFT) algorithms [43] and  
190 allow simulations of large three-dimensional volumes. Here, we employ an FFT spectral  
191 approximation, based on the accelerated scheme [44] and using a special treatment for the  
192 evaluation of the modified Green tensor in the Fourier space [45]. The reader is referred to

1  
2  
3 193 reference [42] for details, whereby a very similar spectral algorithm was developed. We now  
4  
5 194 describe the FFT simulation setup to model the dislocations observed in a thin foil by  
6  
7 195 tomography and obtain their internal stress/strain fields. Figure 4 illustrates the main steps. We  
8  
9 196 consider as an illustrative example a foil of dimension  $960 \text{ nm} \times 960 \text{ nm}$  with a thickness of  
10  
11  $\times 480 \text{ nm}$  shown in figure 4(a). A vertical screw dislocation line which crosses perpendicularly  
12  
13 197 the two surfaces of the foil (threading dislocation) is inserted in the middle of the foil and shown  
14  
15 198 by the solid black line. The FFT grid is here a cube made of  $64 \times 64 \times 64$  voxels. The voxel  
16  
17 199 size, i.e., the spatial resolution of FDM, is set to 15 nm in all simulations. Figure 4(b) shows  
18  
19 200 the associated Nye tensor component  $\alpha_{33}$  distributed on the FFT grid after the “Nye’zation”  
20  
21 201 procedure described above. Note that all dislocation densities are embedded inside the FFT  
22  
23 202 volume. To create the two external free surfaces of the thin foils, where the stress field must  
24  
25 203 satisfy zero-traction boundary conditions, we use a so-called gas phase, which is common in  
26  
27 204 FFT simulations. Voxels with much lower elastic stiffness compose the gas phase. The  
28  
29 205 interfaces between material voxels (with normal stiffness) and gas phase voxels are free  
30  
31 206 surfaces, where the stress field satisfies zero-traction boundary conditions. An example of this  
32  
33 207 gas phase method can be found in reference [42], where the stress field of an edge dislocation  
34  
35 208 line near a pore was simulated and found to agree quantitatively very well with the existing  
36  
37 209 analytical solution. In figure 4(b), one can see how the external free surfaces of the foil are  
38  
39 210 created in the present FDM FFT simulation. Bright voxels compose the foil material, while dark  
40  
41 211 voxels compose the so-called gas phase. More precisely, the elastic stiffness tensor  $\mathbf{C}$  of the  
42  
43 212 olivine material will be attributed to each bright voxel, while a much lower stiffness ( $10^4$  times  
44  
45 213 smaller) is attributed to the dark voxels. In doing so, the internal stresses will be affected near  
46  
47 214 the two free surfaces to satisfy zero-traction boundary conditions. Figure 4(c) shows the internal  
48  
49 215 shear stress field  $\sigma_{23}$  due to the dislocation line in the foil, obtained after convergence of the  
50  
51 216 FDM-FFT numerical algorithm. One can see that it is affected by the external surfaces and  
52  
53  
54  
55  
56  
57  
58  
59  
60

1  
2  
3 218 tends to zero at them. Figure 4(d) also shows the elastic strain  $\epsilon_{12}$  generated near and at the free  
4  
5 219 surfaces to cancel the internal stresses  $\sigma_{13}$  and  $\sigma_{23}$ . A qualitative agreement is observed with  
6  
7 220 elastic fields due to a threading screw dislocation in GaN, simulated by FDM with a finite  
8  
9 221 element approximation [41]. Note finally that because the Nye dislocation density is  
10  
11 222 numerically spread on FFT voxels, dislocation lines have an apparent core in the FDM  
12  
13 223 simulations, with a size the order of the FFT voxel length (15nm), but it is to be interpreted as  
14  
15 224 a numerical core, rather than a physical core. Note that the FDM can be applied to model  
16  
17 225 dislocation cores [46], but it is not the scope of the present work. The spatial resolution is here  
18  
19 226 15nm, much too large to properly describe real dislocation cores. The consequence of having  
20  
21 227 numerical dislocation cores is that the internal stresses are smoothed and not well captured near  
22  
23 228 the physical dislocation cores, but far from the dislocation cores (a few nm) it is correctly  
24  
25 229 rendered. Short-term stress core corrections can be added [38, 39] and are important when  
26  
27 230 dealing with small scale discrete dislocation dynamics, dislocation line tension effects and  
28  
29 231 dislocation reactions. In the present work however, it is not critical and does not alter our  
30  
31 232 findings, as we consider mostly straight dislocation lines separated by distances much larger  
32  
33 233 than the physical core size of dislocations. Furthermore, the resolution (15nm) is already small  
34  
35 234 such that large stresses between dislocation lines can already be predicted (see next section).  
36  
37  
38  
39  
40  
41

42 235 Figure 4  
43

## 44 236 **4 Results and discussion**

### 45 237 **4.1 Dislocation microstructure**

46  
47 238 In order to take an overall look of the PoEM9 microstructure of dislocations, six tilt-series  
48  
49 239 (obtained with the  $22\bar{2}$  diffraction vector) were acquired at a low magnification, which  
50  
51 240 represents an analyzed total area of approximately  $30 \mu\text{m}^2$  [17], with an average angular range  
52  
53 241 from  $-52^\circ$  to  $48^\circ$ .  
54  
55  
56  
57  
58  
59  
60

1  
2  
3 242 Burgers vector indexations are performed using the thickness fringes technique [31] with the  
4  
5 243 004 and  $22\bar{2}$  diffraction vectors (Figures 1 and 2 respectively). They showed that the  
6  
7  
8 244 microstructures are only composed of dislocations with [001] Burgers vectors and  
9  
10 245 overwhelmingly with straight screw dislocation characters. An example of dislocation  
11  
12 246 microstructure obtained in WBDF conditions with the 004 diffraction vector is shown on  
13  
14 247 Figure 1. The electron tomography shows a majority of {110} and (100) glide planes, few  
15  
16  
17 248 cross-slip configurations [17] and colinear interactions [17]. The reconstructed volumes also  
18  
19 249 provide access to  $(\mathbf{u}, \mathbf{b})$  doublets for each dislocation segments, to calculate the Nye tensor,  
20  
21  
22 250 and to simulate the continuous distribution of stress field.  
23  
24 251 Two domains of specimen PoEM9 are studied in detail: zone 1 on Figures 5a-d and zone 2 on  
25  
26 252 Figures 5e-h. A tilt-series composed of 51 micrographs (acquired every  $2^\circ$  with a tilt angle  
27  
28 253 ranging from  $-48^\circ$  to  $+52^\circ$ ) and a second tilt-series of 54 micrographs (acquired every  $2^\circ$  with  
29  
30 254 a tilt angle ranging from  $-56^\circ$  to  $+50^\circ$ ) were obtained in WBDF conditions with the  $22\bar{2}$   
31  
32 255 diffraction vector (zones 1 and 2 respectively). Micrographs from Figures 5a and 5e come from  
33  
34 256 these two tilt-series for a projection angle of  $0^\circ$ . Electron tomography reconstructions enable  
35  
36 257 the characterization of the (110),  $(1\bar{1}0)$  and (100) slip systems which are identified by their  
37  
38 258 colours: white, light grey and black respectively as in Mussi *et al.*, 2015 [17]. Neither the slip  
39  
40 259 systems of the pure screw straight dislocations (coral pink-coloured), nor the habit plane of the  
41  
42 260 red sessile dislocation segment in Figure 5f, can be indexed. Then, the reconstructed volumes  
43  
44 261 are projected along the [001] direction in order to orientate the pure screw dislocations in edge-  
45  
46 262 on position (Figures 5c and 5g) and thereafter, to provide optimal viewing conditions to study  
47  
48 263 the continuous stress distributions.  
49  
50  
51  
52  
53  
54  
55  
56  
57  
58  
59  
60

#### 265 **4.2 Simulation results**

266 The dislocation internal stresses in the thin foil are rotated in the olivine crystal reference frame.  
 267 The  $x_1$ ,  $x_2$  and  $x_3$  directions are now aligned with the  $a$ ,  $b$  and  $c$  directions of the olivine  
 268 orthorhombic unit cell, respectively. In addition to this internal stress, we add the macroscopic  
 269 stress applied experimentally during the compression test (754 MPa) also rotated in the crystal  
 270 reference frame. This is possible since we know the angle between the normal of the thin foil  
 271  $[17\bar{5}12]$  and the compression axis  $[502]$  (approximately  $30^\circ$ ). The total stress field at every  
 272 voxel in the thin foil is then  $\sigma_{ij} = \sigma_{ij}^{int} + \Sigma_{ij}$ , where  $\sigma_{ij}^{int}$  is the local internal stress field due to  
 273 dislocations and  $\Sigma_{ij}$  is the macroscopic stress. It is then possible to project the total stress tensor  
 274 at every voxel on different slip systems using the associated Schmid tensor expressed in the  
 275 olivine orthorhombic reference frame. In the following, we consider three slip systems, labelled  
 276 1, 2 and 3:  $[001](100)$ ,  $[001](110)$  and  $[001](1\bar{1}0)$  respectively. The resolved shear stress  
 277 (RSS) for the three systems are denoted by  $RSS1$ ,  $RSS2$  and  $RSS3$  in the following. They are  
 278 equal to:

$$279 \quad RSS1 = \tau^{[001](100)} = \sigma_{31},$$

$$280 \quad RSS2 = \tau^{[001](110)} = \frac{b}{\sqrt{a^2+b^2}} \sigma_{31} + \frac{a}{\sqrt{a^2+b^2}} \sigma_{32} \approx 90.63 \% \sigma_{31} + 42.26 \% \sigma_{32},$$

$$281 \quad RSS3 = \tau^{[001](1\bar{1}0)} = \frac{b}{\sqrt{a^2+b^2}} \sigma_{31} - \frac{a}{\sqrt{a^2+b^2}} \sigma_{32} \approx 90.63 \% \sigma_{31} - 42.26 \% \sigma_{32}. \quad (9)$$

282 with  $a$  and  $b$  the directions of the olivine orthorhombic unit cell.

283 The macroscopic stress  $\Sigma_{31} = 10ac\sigma / [(5a)^2 + (2c)^2] \approx 302.8$  MPa (with  $a$  and  $c$  the directions  
 284 of the olivine orthorhombic unit cell and  $\sigma$  the applied stress) while  $\Sigma_{32}=0$ . Figures 5 and 6  
 285 show the spatial distribution of the three resolved shear stresses on slices in the thin foil, for the  
 286 two thin foil series. Dislocation lines are shown in figure 5. They are removed in Figure 6 for a  
 287 better comparison of RSS distributions in different slip systems.  $RSS1$ ,  $RSS2$  and  $RSS3$  fields  
 288 look similar, local rotations of RSS patterns (lobes) near dislocations can be seen between the  
 289 three RSS maps. The distribution of the internal elastic energy density  $1/2 \varepsilon_{ij}^e C_{ijkl} \varepsilon_{kl}^e$  is also

1  
2  
3 290 shown in Figure 6. It shows elastic interactions between dislocations (interacting elastic fields  
4  
5 291 between dislocations). Note that the calculation of the mean internal elastic energy within the  
6  
7 292 thin foil volume give  $51.6 \text{ kJ/m}^3$  for series 1 and  $52.2 \text{ kJ/m}^3$  for series 5. The reader is further  
8  
9 293 referred to animations in the supplementary materials, where moving slices parallel to slip  
10  
11 294 planes allow for a better visualization of the long-range elastic interactions between dislocation  
12  
13 295 lines within the thin foils. Histograms of the RSS distributions in the thin foils are provided in  
14  
15 296 Figure 7(a, b) showing a significant heterogeneity of the stress field within the thin foils. One  
16  
17 297 can note that the mean value of RSS1 (302.8 MPa) is slightly larger than that of RSS2 and RSS3  
18  
19 298 (274.4 MPa). This is because the sample was oriented to activate system 1 preferentially. Strong  
20  
21 299 variations in the stress values can be seen, typically  $\pm 400 \text{ MPa}$  around the mean values.  
22  
23 300 Regions with local stresses reaching 1 GPa are also observed, particularly nearby dislocation  
24  
25 301 dipoles. Finally, Figure 7(c) shows cumulative distribution functions (CDF) for RSS1, RSS2,  
26  
27 302 RSS3, for the two thin foil series, with RSS values extracted only at the dislocation lines  
28  
29 303 (instead of taking values at all voxels in the thin foils). In doing so, we only consider dislocation  
30  
31 304 driving stresses in the single crystal. The CDF are centred about zero. Broad distributions, with  
32  
33 305 again variations up to  $\pm 400 \text{ MPa}$ , are clearly evidenced in the CDF for the three slip systems  
34  
35 306 and the two thin foils, and they look rather similar. One clear feature in all these maps and  
36  
37 307 distributions is thus the presence of long-range elastic interactions between dislocations and  
38  
39 308 significant local variations of the RSS values in the three systems considered due to the  
40  
41 309 complexity of the three-dimensional stress state.  
42  
43  
44  
45  
46  
47  
48  
49  
50

## 51 311 **4.2 Discussion**

52 312 The present coupled electron tomography/FDM analysis allows obtaining for the first time a  
53  
54 313 detailed, three-dimensional, physical/mechanical description of dislocation networks in the  
55  
56 314 studied thin foils. A physical description of dislocations (Burgers vectors, 3D arrangement of  
57  
58  
59  
60



1  
2  
3 315 dislocation lines, junctions, dipoles, networks) is complemented by a mechanical description  
4  
5 316 (strains, rotations, stresses, energy). In the present study, we specifically discuss two points, (1)  
6  
7 317 the possible activation of different slip systems in olivine deformed at low temperature due to  
8  
9 318 the complexity of the three-dimensional stress state, and (2), the history of dislocation dynamics  
10  
11 319 and the associated build-up of polarized internal stresses and kinematic hardening in single  
12  
13 320 crystals at the nanometre scale.  
14  
15  
16

17 321  
18  
19 322 (1) Activation of slip systems: The POEM-9 specimen, from which thin foils have been  
20  
21 323 extracted and analysed here, was compressed along the [502] direction, to preferentially  
22  
23 324 activate the [001](100) slip system (system 1 and RSS1). However, an uncertainty between  
24  
25 325 the possible activated slip systems was mentioned [29]. Another system, [001](110) was also  
26  
27 326 proposed as a possible system. A third system could also be activated, [001](1 $\bar{1}$ 0). They  
28  
29 327 correspond to system 2 and system 3 in the present study. Our distributions of RSS values in  
30  
31 328 the thin foil indeed suggest that system 1 is only slightly favoured as compared to systems 2  
32  
33 329 and 3, because the mean value of RSS1 is only slightly larger (difference of less than 30 MPa).  
34  
35 330 However, in a recent work [17], systems 2 and 3 are observed to be easier to activate (lower  
36  
37 331 CRSS) than system 1, system 1 being the second easiest system to activate after system 2 and  
38  
39 332 3. As such it is not easy to say which one of system 1 or systems (2, 3) was preferentially  
40  
41 333 activated in our studied sample. The distributions of the RSS values extracted only at  
42  
43 334 dislocation lines are certainly more speaking. Indeed, the distributions show very similar  
44  
45 335 features for all series and slip systems. More precisely, they are all broad and show significant  
46  
47 336 local variations,  $\pm 400$  MPa. As such, the slight difference of the mean RSS between system 1  
48  
49 337 and systems (2, 3), less than 30 MPa, becomes negligible as compared to possible large local  
50  
51 338 values of RSS. From this, we can conclude that, although POEM-9 was compressed in a way  
52  
53  
54  
55  
56  
57  
58  
59  
60

339 to favor slip system 1, the three systems can all be activated, because of the strong heterogeneity  
340 of the internal stress field.

341

342 (2) Internal stresses and kinematic hardening: The simulated fields of RSS show a significant  
343 heterogeneity. Recently, an experimental work on deformed olivine single crystals and  
344 polycrystals using High-Resolution-EBSD (HR-EBSD) revealed a pronounced heterogeneity  
345 in the in-plane elastic shear strains and shear stresses at the surface [47, 48]. Variations up to  
346  $\pm 1$  GPa around the mean value were reported in both polycrystals and single crystals (at low  
347 temperatures) at the micron scale. Such polarization and patterning of internal, intragranular  
348 and intergranular stresses, can be related to the build-up of geometrically necessary dislocation  
349 densities. Strong heterogeneity of internal stresses is to be associated with kinematic hardening.  
350 In the present study, we can look at the heterogeneity of internal stresses down to the scale of  
351 typical HR-EBSD map pixels, *i.e.*, at the nanometre scale. Our results also reveal a significant  
352 heterogeneity of internal stresses at the nanometre scale in a single crystal containing  
353 dislocation networks. Distributions of RSS show broad profiles, with variations up to  $\pm 400$   
354 MPa around the mean value. Interestingly, the histograms show a few negative RSS values.  
355 The results thus suggest that kinematic hardening has been built-up and is a signature of the  
356 past dynamics of dislocations observed.

357

358 The application of our electron tomography/FDM method brings valuable insights regarding  
359 the complexity of plastic flow in olivine. In a simple single crystal subjected to simple  
360 compression loading, it shows that plastic anisotropy and activation of dislocation slip systems  
361 can be significantly altered by the large fluctuations of the local mechanical fields. Furthermore,  
362 it evidences the built-up of kinematic hardening. This plastic behaviour observed at the single  
363 crystal, nanometre scale, certainly has a strong impact on the rheology of olivine polycrystals

1  
2  
3 364 within the Earth's mantle. More generally, our proposed analysis method can also be employed  
4  
5 365 to investigate other mechanisms and defects typically investigated in the TEM for various  
6  
7 366 crystals, such as subgrain boundaries, dislocation networks, dislocation grain boundary  
8  
9 367 interactions, dislocation reactions, interactions between dislocations and pores/precipitates etc.  
10  
11 368 Furthermore, as shown in Figure 8, the method also provides elastic fields in the vicinity of and  
12  
13 369 at free surfaces, which allows making links between elastic fields measurements using  
14  
15 370 experimental techniques such as precession electron diffraction [49], HR-EBSD (high-  
16  
17 371 resolution electron backscatter diffraction), HR-TKD (high-resolution transmission Kikuchi  
18  
19 372 diffraction) [41], ACOM (automated crystal orientation mapping) ASTAR<sup>®</sup> [50] and defects  
20  
21 373 inside the material. It must be emphasized that, in addition to provide 3D anisotropic elastic  
22  
23 374 fields, our approach allows a spatial resolution of 15 nm in routine use, extendable down to 5  
24  
25 375 nm. The method can also be used to assess the accuracy of HR-TKD, or ACOM/ASTAR  
26  
27 376 methods, when measuring the elastic fields around dislocation structures.  
28  
29  
30  
31  
32

33 377

## 34 35 378 **5 Conclusion**

36  
37 379 In this contribution, we propose an original experimental and theoretical characterization  
38  
39 380 method for studying dislocation networks in crystalline materials. The method combines  
40  
41 381 dislocation electron tomography, which provides a three-dimensional characterization of  
42  
43 382 dislocation lines and Burgers vectors, to a field dislocation mechanics model, which provides  
44  
45 383 the associated internal mechanical fields. To demonstrate the potential of our method, we have  
46  
47 384 considered single crystal thin foils extracted from a compressed olivine single crystal. Our  
48  
49 385 results have revealed significant local fluctuations in the local mechanical fields, particularly  
50  
51 386 the resolved shear stresses in different slip systems, which certainly play a role in the strong  
52  
53 387 anisotropy of olivine and the activation of different dislocation slip systems. Our first results  
54  
55 388 have also evidenced the built-up of kinematic hardening at the nanometre scale in a single  
56  
57  
58  
59  
60

389 crystal. Our method has a considerable potential for studying various types of dislocation  
390 microstructures and plastic deformation mechanisms in different crystals

391

### 392 **Acknowledgments**

393 This project has received funding from the European Research Council (ERC) under the European  
394 Union's Horizon 2020 research and innovation program under grant agreement No 787198 –  
395 TimeMan. AM, VT and AG would like to acknowledge support from the French national research  
396 agency (ANR) through the grant ANR-PRC-2022-MAMIE-NOVA (ANR-22-CE08-0018). The TEM  
397 national facility in Lille (France) is supported by the Conseil Regional du Nord-Pas de Calais, the  
398 European Regional Development Fund (ERDF), and the Institut National des Sciences de l'Univers  
399 (INSU, CNRS).

400

### 401 **References**

- 402 [1] Kubin LP, Dislocations, Mesoscale Simulations and Plastic Flow, Oxford Series on  
403 Materials Modelling (Oxford, 2013; online edn, Oxford Academic, 23 May 2013). doi:  
404 10.1093/acprof:oso/9780198525011.001.0001.
- 405 [2] Devincere B, Kubin LP (1997). The modelling of dislocation dynamics: elastic behaviour  
406 versus core properties. *Philos. Trans. R. Soc. A-Math. Phys. Eng. Sci.*, 355 (1731), 2003–2012.  
407 doi: 10.1098/rsta.1997.0102
- 408 [3] Devincere B, Kubin LP, Hoc T (2006). Physical analyses of crystal plasticity by DD  
409 simulations *Scr. Mater.*, 54 (5), 741-746. doi: 10.1016/j.scriptamat.2005.10.066.
- 410 [4] Barnard JS, Sharp J, Tong JR & Midgley PA (2006a). High-resolution three-  
411 dimensional imaging of dislocations. *Science* 313(5785), 319–319. doi:  
412 10.1116/science.1125783.

- 1  
2  
3 413 [5] Sharp JH, Barnard JS, Kaneko K, Higashida K & Midgley PA (2008). Dislocation  
4  
5 414 tomography made easy: A reconstruction from ADF STEM images obtained using automated  
6  
7 415 image shift correction. *J Phys* 126, 1–4. doi: 10.1088/1742-6596/126/1/012013.  
8  
9  
10 416 [6] Tanaka M, Higashida K, Kaneko K, Hata S & Mitsuhashi M (2008). Crack tip  
11  
12 417 dislocations revealed by electron tomography in silicon single crystal. *Scr Mater* 59, 901–904.  
13  
14 418 doi: 10.1016/j.scriptamat.2008.06.042.  
15  
16  
17 419 [7] Feng ZQ, Lin CW, Li TT, Luo X, Wu GL, Huang XX (2017). Electron tomography of  
18  
19 420 dislocations in an Al-Cu-Mg alloy. *IOP Conf. Series: Materials Science and Engineering* 219,  
20  
21 421 012018. doi: 10.1088/1757-899X/219/1/012018.  
22  
23  
24 422 [8] Mussi, A., Addad, A., Onimus, F. (2021a). Dislocation electron tomography: A  
25  
26 423 technique to characterize the dislocation microstructure evolution in zirconium alloys under  
27  
28 424 irradiation, *Acta Mater.* 213, 116964. doi: 10.1016/j.actamat.2021.116964.  
29  
30  
31 425 [9] Mussi A, Carrez P, Gouriet K, Hue B & Cordier P (2021b). 4D electron tomography of  
32  
33 426 dislocations undergoing electron irradiation. *C R Phys* 22 (S3), 67–81. doi: 10.5802/crphys.80.  
34  
35  
36 427 [10] Mussi, A., Cordier, P., Demouchy, S., 2015a. Characterization of dislocation  
37  
38 428 interactions in olivine using electron tomography. *Philos. Mag.* 95, 335–345. doi:  
39  
40 429 10.1080/14786435.2014.1000996.  
41  
42  
43 430 [11] Kacher JP, Liu GS & Robertson IM (2011). Visualization of grain boundary/dislocation  
44  
45 431 interactions using tomographic reconstructions. *Scr Mater* 64, 677–680. doi:  
46  
47 432 10.1016/j.scriptamat.2010.12.020.  
48  
49  
50 433 [12] Kacher J & Robertson IM (2012). Quasi-four-dimensional analysis of dislocation  
51  
52 434 interactions with grain boundaries in 304 stainless steel. *Acta Mater* 60, 6657–6672. doi:  
53  
54 435 10.1016/j.actamat.2012.08.036.  
55  
56  
57  
58  
59  
60

- 1  
2  
3 436 [13] Kacher J & Robertson IM (2014). In situ and tomographic analysis of dislocation/ grain  
4  
5 437 boundary interactions in  $\alpha$ -titanium. *Philos Mag* 94(8), 814–829. doi:  
6  
7 438 10.1080/14786435.2013.868942.
- 8  
9  
10 439 [14] Chen S & Yu Q (2019). The role of low angle grain boundary in deformation of titanium  
11  
12 440 and its size effect. *Scr Mater* 163, 148–151. doi: 10.1016/j.scriptamat.2018.10.054.
- 13  
14 441 [15] Mussi, A., Cordier, P., Ghosh, S., Garvik, N., Nzogang, B.C., Carrez, P., Garruchet, S.,  
15  
16 442 2016. Transmission electron microscopy of dislocations in cementite deformed at high pressure  
17  
18 443 and high temperature. *Philos. Mag.* 96, 1773–1789. doi: 10.1080/14786435.2016.1177670.
- 19  
20 444 [16] Mussi A, Cordier P, Demouchy S & Vanmansart C (2014). Characterization of the glide  
21  
22 445 planes of the [001] screw dislocations in olivine using electron tomography. *Phys Chem*  
23  
24 446 *Minerals* 41, 537–545. doi: 10.1007/s00269-014-0665-1.
- 25  
26 447 [17] Mussi, A., Nafi, M., Demouchy, S., Cordier, P., 2015b. On the deformation mechanism  
27  
28 448 of olivine single crystals at lithospheric temperatures: an electron tomography study. *Eur. J.*  
29  
30 449 *Mineral.* 27, 707–715. doi: 10.1127/ejm/2015/0027-2481.
- 31  
32 450 [18] Mussi A, Cordier P, Demouchy S & Hue B (2017). Hardening mechanisms in olivine  
33  
34 451 single crystal deformed at 1090°C: An electron tomography study. *Philos Mag* 97(33), 3172–  
35  
36 452 3185. doi: 10.1080/14786435.2017.1367858.
- 37  
38 453 [19] Mussi A, Gallet J, Castelnau O & Cordier P (2021c). Application of electron  
39  
40 454 tomography of dislocations in beam-sensitive quartz to the determination of strain components.  
41  
42 455 *Tectonophysics* 803, 228754. doi: 10.1016/j.tecto.2021.228754.
- 43  
44 456 [20] Liu GS, House SD, Kacher J, Tanaka M, Higashida K & Robertson IM (2014). Electron  
45  
46 457 tomography of dislocation structures. *Mater Charact* 87, 1–11. doi:  
47  
48 458 10.1016/j.matchar.2013.09.016.
- 49  
50  
51  
52  
53  
54  
55  
56  
57  
58  
59  
60

- 1  
2  
3 459 [21] Feng Z, Fu R, Lin C, Wu G, Huang T, Zhang L & Huang X (2020). TEM-based  
4  
5 460 dislocation tomography: Challenges and opportunities. *Curr Opin Solid State Mater Sci* 24, 1–  
6  
7 461 9. doi: 10.1016/j.cossms.2020.100833.
- 8  
9  
10 462 [22] Hata S, Furukawa H, Gondo T, Hirakami D, Horii N, Ikeda K-I, Kawamoto K, Kimura  
11  
12 463 K, Matsumura S, Mistuhara M, Miyazaki H, Miyazaki S, Murayama MM, Nakashima H, Saito  
13  
14 464 H, Sakamoto M & Yamazaki S (2020a). Electron tomography imaging methods with diffraction  
15  
16 465 contrast for materials research. *Microscopy* 69(3), 141–155. doi: 10.1093/jmicro/dfaa002.
- 17  
18  
19 466 [23] Hata S, Honda T, Saito H, Mitsuhara M, Petersen TC & Murayama M (2020b). Electron  
20  
21 467 tomography: An imaging method for materials deformation dynamics. *Curr Opin Solid State*  
22  
23 468 *Mater Sci* 24, 1–12. doi: 10.1016/j.cossms.2020.100850.
- 24  
25  
26 469 [24] Eftink BP, Gray GT & Maloy SA (2017). Stereographic methods for 3D  
27  
28 470 characterization of dislocations. *Microsc Microanal* 23, 210–211. doi:  
29  
30 471 10.1017/S1431927617001738.
- 31  
32  
33 472 [25] Jácome LA, Pöthkow K, Paetsch O & Hege H-C (2018). Three-dimensional  
34  
35 473 reconstruction and quantification of dislocation substructures from transmission electron  
36  
37 474 microscopy stereo pairs. *Ultramicroscopy* 195, 157–170. doi : 10.1016/j.ultramic.2018.08.015.
- 38  
39  
40 475 [26] Oveisi E, Letouzey A, Alexander DTL, Jeangros Q, Schäublin R, Lucas G, Fua P,  
41  
42 476 Hébert C (2017). Tilt-less 3-D electron imaging and reconstruction of complex curvilinear  
43  
44 477 structures. *Sci Rep* 7, 10630. doi: 10.1038/s41598-017-07537-6.
- 45  
46  
47 478 [27] Oveisi E, Letouzey A, Zanet SD, Lucas G, Cantoni M, Fua P & Hébert C (2018). Stereo-  
48  
49 479 vision three-dimensional reconstruction of curvilinear structures imaged with a TEM.  
50  
51 480 *Ultramicroscopy* 184, 116–124. doi: 10.1016/j.ultramic.2017.08.010.
- 52  
53  
54 481 [28] Altingövde O, Mishchuk A, Ganeeva G, Oveisi E, Hebert C, Fua P (2022). 3D  
55  
56 482 reconstruction of curvilinear structures with stereomatching deep convolutional neural  
57  
58 483 networks. *Ultramicroscopy* 234, 113460. doi: 10.1016/j.ultramic.2021.113460.
- 59  
60

- 1  
2  
3 484 [29] Demouchy S, Tommasi A, Boffa Ballaran T, Cordier P (2013). Low strength of Earth's  
4  
5 485 uppermost mantle inferred from tri-axial deformation experiments on olivine crystals. *Phys.*  
6  
7 486 *Earth Planet. Int.* 220, 37-49. doi: 10.1016/j.pepi.2013.04.008.
- 8  
9  
10 487 [30] Paterson, MS (1990) Rock deformation experimentation, in: Duba, A. *et al.* (Eds.), *The*  
11  
12 488 *Brittle-Ductile Transition in Rocks: the Head Volume*. Geophys. Monogr. Ser., AGU,  
13  
14 489 Washington D.C., pp. 187–194
- 15  
16  
17 490 [31] Ishida Y, Ishida H, Kohra K, Ichinose H (1980). Determination of the Burgers vector of  
18  
19 491 a dislocation by weak-beam imaging in a HVEM. *Phil. Mag. A*, 42, 453–462. doi:  
20  
21 492 10.1080/01418618008239369.
- 22  
23  
24 493 [32] Miyajima N, Walte N (2009). Burgers vector determination in deformed perovskite and  
25  
26 494 post-perovskite of CaIrO<sub>3</sub> using thickness fringes in weak-beam dark-field images,  
27  
28 495 *Ultramicroscopy*, 109, 683-692. doi: 10.1016/j.ultramic.2009.01.010.
- 29  
30  
31 496 [33] Rebled, J. M., Yedra, L., Estrade, S., Portillo, J., & Peiro, F. (2011). A new approach  
32  
33 497 for 3D reconstruction from bright field TEM imaging: Beam precession assisted electron  
34  
35 498 tomography. *Ultramicroscopy*, 111(9-10), 1504-1511. doi.org/10.1016/j.ultramic.2011.06.002.
- 36  
37  
38 499 [34] Herman GT, Lakshminarayanan AV, Naparstek A (1976). Convolution reconstruction  
39  
40 500 techniques for divergent beams. *Comput. Biol. Med.* 6, 259–271. doi: 10.1016/0010-  
41  
42 501 4825(76)90065-2.
- 43  
44  
45 502 [35] Pettersen EF, Goddard TD, Huang CC, Couch GS, Greenblatt DM, Meng EC, Ferrin  
46  
47 503 TE (2004). UCSF Chimera: a visualization system for exploratory research and analysis. *J.*  
48  
49 504 *Comput. Chem.* 25, 1605–1612. doi: 10.1002/jcc.20084.
- 50  
51  
52 505 [36] Acharya A (2001). A model of crystal plasticity based on the theory of continuously  
53  
54 506 distributed dislocations. *J. Mech. Phys. Solids* 49, 761-784. doi: 10.1016/S0022-  
55  
56 507 5096(00)00060-0.
- 57  
58  
59  
60

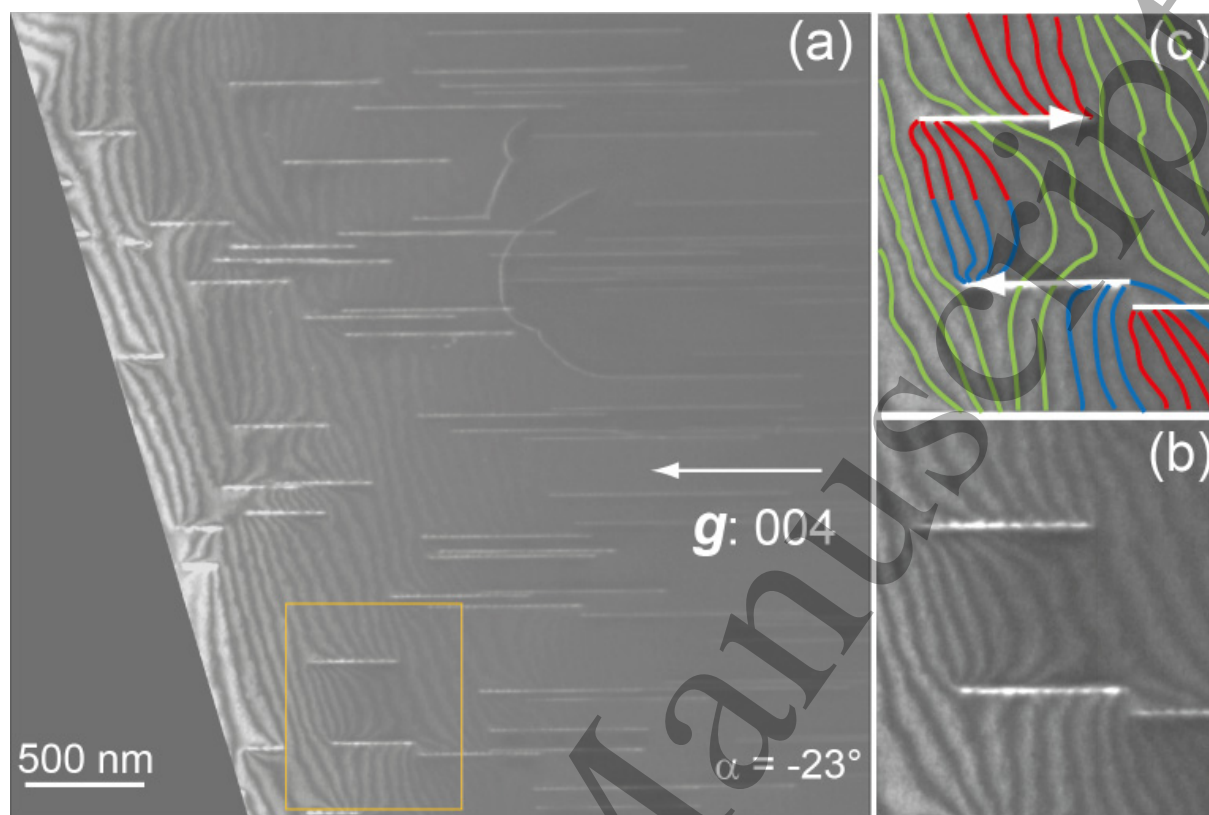


- 1  
2  
3 508 [37] Nye JF (1953). Some geometrical relations in dislocated crystals. *Acta Metall.* 1, 153-  
4  
5 509 162. doi: 10.1016/0001-6160(53)90054-6.  
6  
7 510 [38] Bertin N (2019). Connecting discrete and continuum dislocation mechanics: A non-  
8  
9 511 singular spectral framework. *Int. J. Plasticity* 122, 268-284. doi: 10.1016/j.ijplas.2018.12.006.  
10  
11 512 [39] Kohnert AA, Capolungo L (2021). Spectral discrete dislocation dynamics with  
12  
13 513 anisotropic short range interactions. *Comput. Mater. Sci.* 189, 110243. doi:  
14  
15 514 10.1016/j.commatsci.2020.110243.  
16  
17 515 [40] Arora R, Zhang X, Acharya A (2020). Finite element approximation of finite deformation  
18  
19 516 dislocation mechanics. *Comput. Methods Appl. Mech. Eng.* 367, 113076. doi:  
20  
21 517 10.1016/j.cma.2020.113076.  
22  
23 518 [41] Ernould C, Taupin V, Beausir B, Fundenberger JJ, Maloufi N, Guyon J, Bouzy E (2022).  
24  
25 519 Characterization of a nanopipe dislocation in GaN by means of HR-EBSD and field dislocation  
26  
27 520 mechanics analysis. *Mater. Charac.* 194, 112351. doi: 10.1016/j.matchar.2022.112351.  
28  
29 521 [42] Djaka KS, Villani A, Taupin V, Capolungo L, Berbenni S (2017). Field Dislocation  
30  
31 522 Mechanics for heterogeneous elastic materials: A numerical spectral approach. *Comput.*  
32  
33 523 *Methods Appl. Mech. Engrg.* 315, 921-942. doi: 10.1016/j.cma.2016.11.036.  
34  
35 524 [43] Frigo M, Johnson SG (2005). The Design and Implementation of FFTW3. *Proceedings*  
36  
37 525 *of the IEEE* 93, 216-231. doi: 10.1109/JPROC.2004.840301.  
38  
39 526 [44] Michel JC, Moulinec H, Suquet P (2001). A computational scheme for linear and non-  
40  
41 527 linear composites with arbitrary phase contrast. *Internat. J. Numer. Methods Engrg.* 52, 139-  
42  
43 528 160. doi: 10.1002/nme.275.  
44  
45 529 [45] Willot F (2015). Fourier-based schemes for computing the mechanical response of  
46  
47 530 composites with accurate local fields. *C. R. Mec* 343, 232-245. doi:  
48  
49 531 10.1016/j.crme.2014.12.005.  
50  
51  
52  
53  
54  
55  
56  
57  
58  
59  
60

- 1  
2  
3 532 [46] Zhang X, Acharya A, Walkington NJ, Bielak J (2015). A single theory for some quasi-  
4  
5 533 static, supersonic, atomic, and tectonic scale applications of dislocations. *J. Mech. Phys. Solids*  
6  
7 534 84, 145-195. doi: 10.1016/j.jmps.2015.07.004
- 8  
9  
10 535 [47] Wallis D, Hansen LN, Kumamoto KM, Thom CA, Plümper O, Ohl M, Durham WB,  
11  
12 536 Goldsby DL, Armstrong DEJ, Meyers CD, Goddard RM, Warren JM, Breithaupt T, Drury MR,  
13  
14 537 Wilkinson AJ (2020). Dislocation interactions during low-temperature plasticity of olivine and  
15  
16 538 their impact on the evolution of lithospheric strength. *Earth Planet. Sci. Letters* 543, 116349.  
17  
18 539 doi: 10.1016/j.epsl.2020.116349.
- 19  
20  
21 540 [48] Wallis D, Hansen LN, Wilkinson AJ, Lebensohn RA (2021). Dislocation interactions in  
22  
23 541 olivine control postseismic creep of the upper mantle. *Nature Communications* 12, 3496. doi:  
24  
25 542 10.1038/s41467-021-23633-8.
- 26  
27  
28 543 [49] Cooper D, Bernier N, Rouvière JL (2015). Combining 2 nm spatial resolution and 0.02%  
29  
30 544 precision for deformation mapping of semiconductor specimens in a transmission electron  
31  
32 545 microscope by precession electron diffraction. *Nano Lett.* 15, 5289–5294. doi:  
33  
34 546 10.1021/acs.nanolett.5b01614.
- 35  
36  
37 547 [50] Després A, Veron M (2023). Elastic strain field measurements in the TEM for  
38  
39 548 metallurgical applications. *Mater. Charact.* 202, 113012. doi: 10.1016/j.matchar.2023.113012.  
40  
41  
42 549  
43  
44 550

551 **Figures**

552

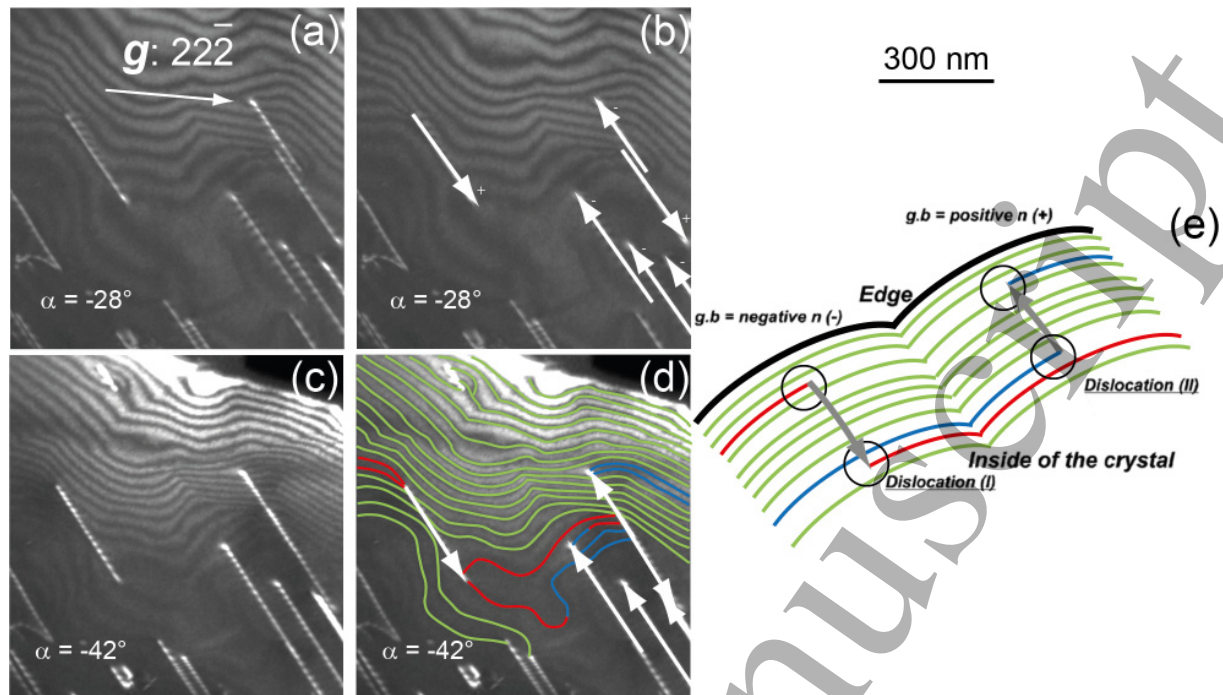


553

554 **Figure 1:** WBDF micrograph obtained with the 004 diffraction vector: (a) Global micrograph  
 555 where thickness fringes are clearly seen; (b) enlargement of a dislocation dipole pointed out by  
 556 an orange rectangle on Figure 1(a) ; (c) enlargement of the dipole where the unterminated  
 557 thickness fringes are coloured in green, the terminated thickness fringes are coloured in red at  
 558 the extremities of the dislocations represented with arrows oriented on the opposite direction of  
 559 the wedge, and the terminated thickness fringes are coloured in blue at the extremities of the  
 560 dislocation represented with an arrow oriented on the direction of the wedge (the directions of  
 561 the arrows are linked with the signs of the Burgers vectors).

Accepted Manuscript

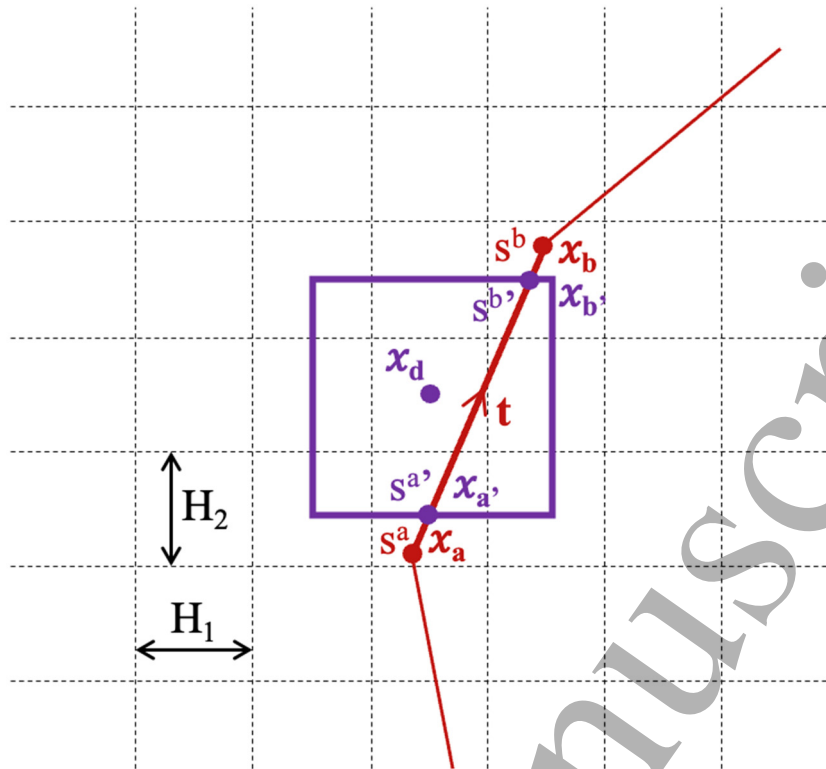
562



563

564 **Figure 2:** Association of the intensity of the dislocation extremities with the sign of the Burgers  
 565 vector: (a) Raw micrograph in WBDF conditions, obtained with the  $22\bar{2}$  diffraction vector (with  
 566 a projection angle of  $-28^\circ$ ), where an intensity asymmetry of dislocation extremities is clearly  
 567 seen; (b) arrows added on the raw micrograph of Figure 2(a) = the arrow is oriented in the  
 568 direction of the intense extremity of the dislocation; (c) raw micrograph of the same domain  
 569 with a projection angle of  $-42^\circ$ ; (d) arrows and thickness fringes added and redrawn on the raw  
 570 micrograph of Figure 2(c) where the thickness fringes are coloured in green when they are not  
 571 terminated on the extremities of dislocations, in red at the extremities of the dislocations  
 572 represented with arrows oriented on the opposite direction of the wedge, and in blue at the  
 573 extremities of the dislocation represented with an arrow oriented on the direction of the wedge;  
 574 (e) cartoon extracted from Miyajima & Walte [32], where the method to get access to the  $\mathbf{g} \cdot \mathbf{b}$   
 575 product is described, taking into account the signs of the Burgers vectors, following Ishida *et*  
 576 *al.* [31], with the same color code and arrow direction code as Figure 2(d). A link between the  
 577 intensity of the dislocation extremities and the sign of the Burgers vector is noticeably evident.

60

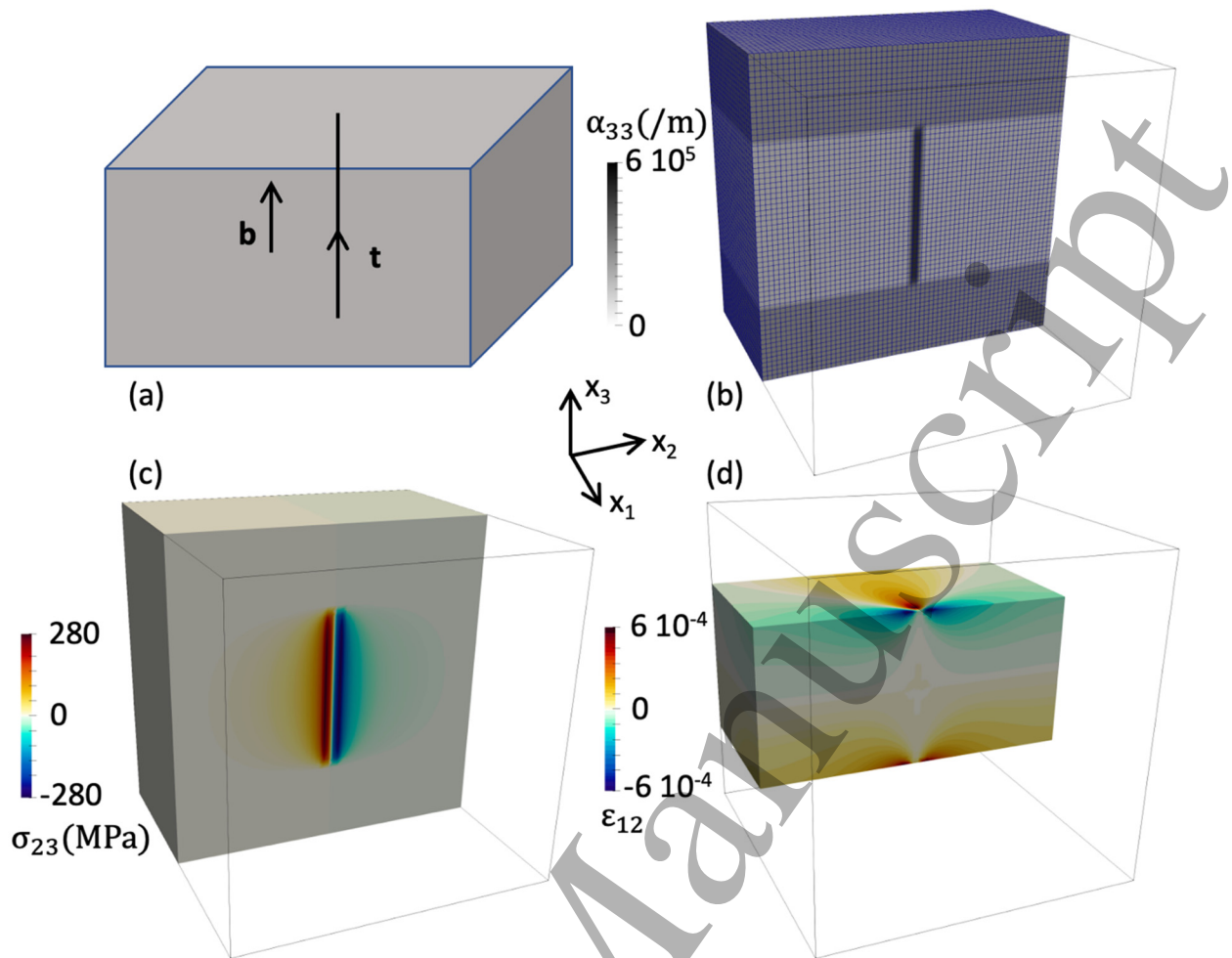


578

579 **Figure 3:** Illustration of the method used to assign a Nye dislocation density at a voxel  $x_d$  due  
 580 to a dislocation segment. See text for details.

581

Accepted Manuscript

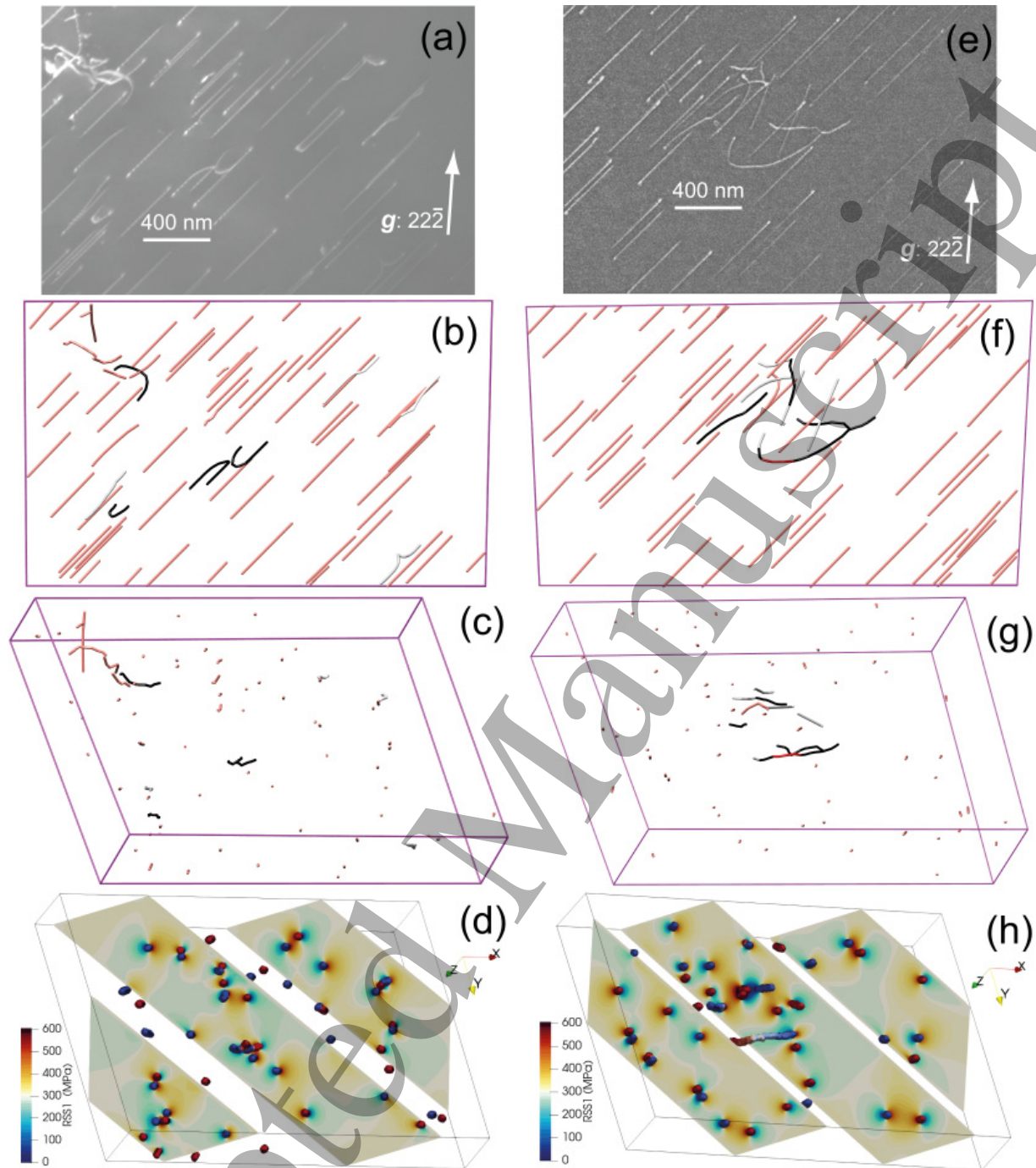


582

583 **Figure 4:** Numerical strategy to model the stress field of discrete dislocation lines observed by  
 584 tomography in a thin foil. (a) Sketch of a thin foil containing one vertical threading screw  
 585 dislocation line (black solid line, the line and Burgers vectors are also indicated). (b)  
 586 Corresponding Nye tensor screw component  $\alpha_{33}$  on the 3D FFT grid (clip). Bright voxels  
 587 belong to the thin foil while dark voxels correspond to the gas phase. (c) Internal shear stress  
 588 field  $\sigma_{23}$ . (d) Elastic strain field  $\epsilon_{12}$  generated near and at the free surfaces of the thin foil to  
 589 cancel the internal stresses  $\sigma_{13}$  and  $\sigma_{23}$  at the free surfaces. The coordinate system used for  
 590 figures (b, c, d) is shown at the centre of the figure.

591  
592  
593  
594  
595  
596  
597  
598  
599  
600

591



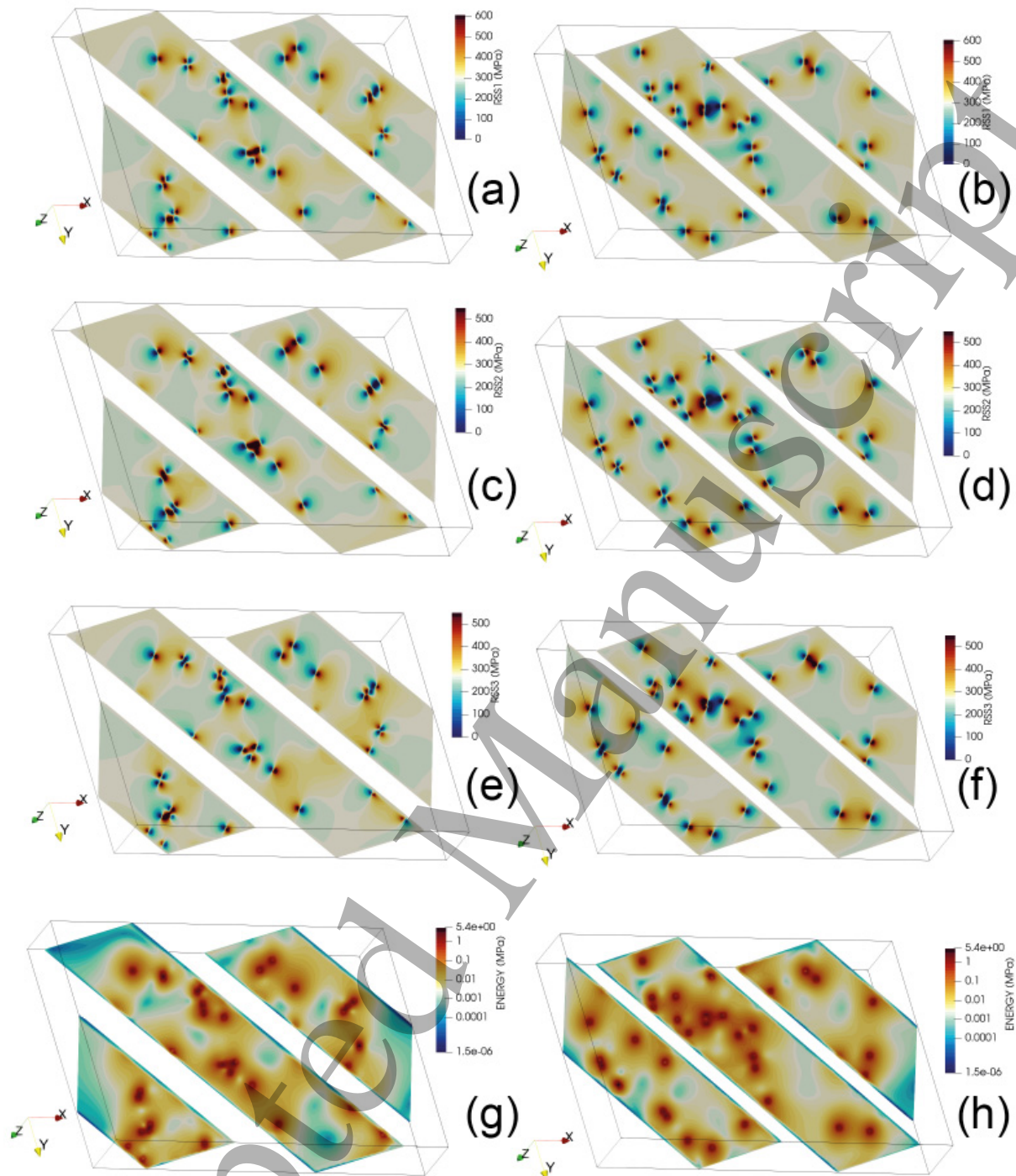
592

593 **Figure 5:** Link between TED and FDM: (a) Raw micrograph in WBDF conditions, obtained  
 594 with the  $22\bar{2}$  diffraction vector (with a projection angle of  $0^\circ$ ) of zone 1; (b) reconstructed  
 595 volume of the same domain with the same projected angle (the (110),  $(\bar{1}10)$  and (100) slip  
 596 systems are respectively colored in white, light grey and black as in [17]); (c) reconstructed  
 597 volume of the same domain along the [001] direction; (d) Spatial distributions (3 slices) of  
 598 RSS1 in series 1 obtained along the same orientation as Figure 5(c) located in the interaction

1  
2  
3 599 between the two black dislocations in the middle of the micrograph in Figures 5(a-b)  
4  
5 600 (Dislocation lines are also shown and coloured w.r.t. their sign.); (e) raw micrograph in WBDF  
6  
7 601 conditions, obtained with the  $22\bar{2}$  diffraction vector (with a projection angle of  $0^\circ$ ) of zone 2;  
8  
9 602 (f) reconstructed volume of the same domain with the same projected angle (the  $(1\bar{1}0)$  and  
10  
11 603  $(100)$  slip systems are respectively colored in light grey and black); (g) reconstructed volume  
12  
13 604 of the same domain along the  $[001]$  direction; (h) Spatial distributions (3 slices) of RSS1 in  
14  
15 605 series 5 obtained along the same orientation as Figure 5(g) located in the red dislocation  
16  
17 606 segment (Dislocation lines are also shown and coloured with reference to their sign).  
18  
19  
20  
21  
22  
23  
24  
25  
26  
27  
28  
29  
30  
31  
32  
33  
34  
35  
36  
37  
38  
39  
40  
41  
42  
43  
44  
45  
46  
47  
48  
49  
50  
51  
52  
53  
54  
55  
56  
57  
58  
59  
60

Accepted Manuscript





608

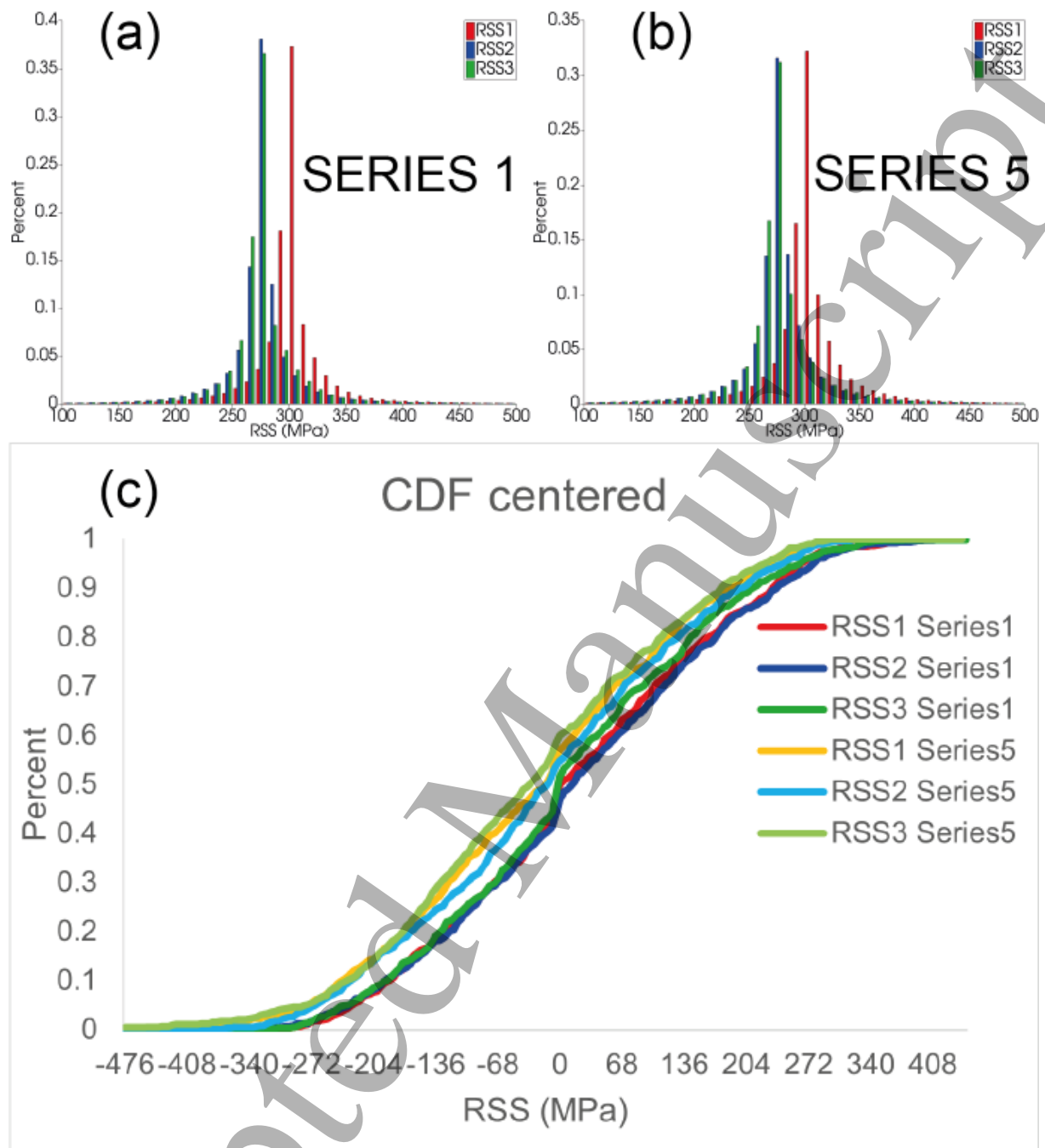
609 **Figure 6:** Spatial distributions (3 slices) of RSS1 (a, b), RSS2 (c, d), RSS3 (e, f) and elastic

610 energy density (g, h) for series 1 (left column) and series 5 (right column).

611

ACCEPTED

612



613

614 **Figure 7:** Distributions of RSS1, RSS2 and RSS3 for series 1 (zone 1) and series 5 (zone 2).

615 (a, b): All RSS values in the thin foils are used. (c): Only RSS values at dislocation lines are

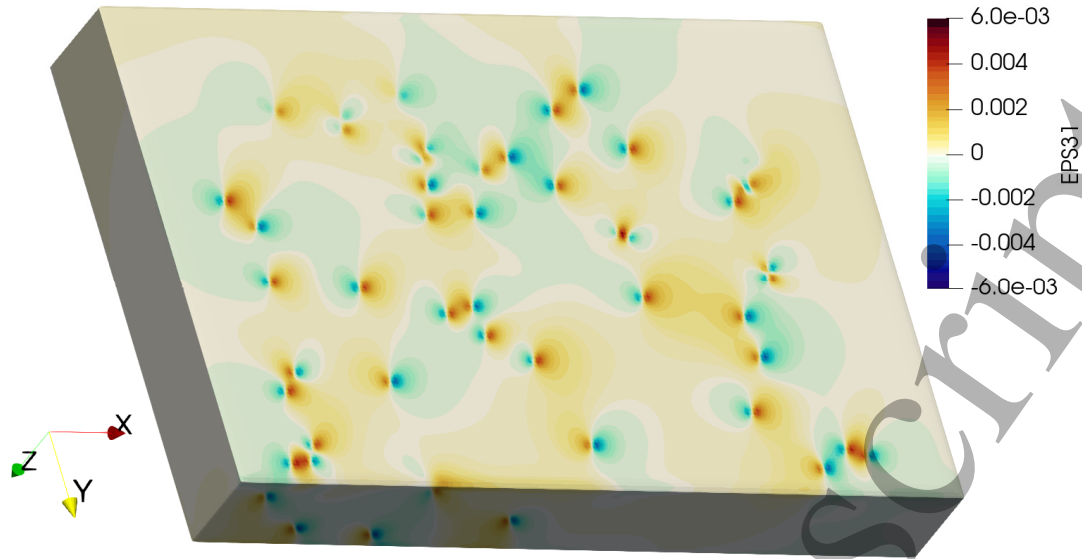
616 used. All cumulative distribution functions (CDF) for the three slip systems and the two series

617 are superimposed on the same figure.

618

59

60



619

620 **Figure 8:** Elastic strain  $\epsilon_{31}$  at the surface of the thin foil for series 1.

Accepted Manuscript